





## Coherent spin dynamics of rare-earth doped crystals in the high-cooperativity regime

Joseph Alexander <sup>1,\*</sup> Gavin Dold <sup>1,2</sup> Oscar W. Kennedy,<sup>1</sup> Mantas Šimėnas <sup>1</sup> James O’Sullivan <sup>1</sup>  
 Christoph W. Zollitsch,<sup>1</sup> Sacha Welinski,<sup>3,4</sup> Alban Ferrier,<sup>3,5</sup> Eloise Lafitte-Houssat,<sup>3,4</sup> Tobias Lindström,<sup>2</sup>  
 Philippe Goldner,<sup>3</sup> and John J. L. Morton<sup>1,6,†</sup>

<sup>1</sup>*London Centre for Nanotechnology, University College London, London WC1H 0AH, United Kingdom*


<sup>2</sup>*National Physical Laboratory, Hampton Road, Teddington TW11 0LW, United Kingdom*

<sup>3</sup>*Université PSL, Chimie ParisTech, CNRS, Institut de Recherche de Chimie Paris, 75005 Paris, France*

<sup>4</sup>*Thales Research and Technology, 1 Avenue Augustin Fresnel, 91767 Palaiseau, France*

<sup>5</sup>*Faculté des Sciences et Ingénierie, Sorbonne Université, 75005 Paris, France*

<sup>6</sup>*Department of Electronic and Electrical Engineering, UCL, London WC1E 7JE, United Kingdom*

 (Received 28 June 2022; revised 17 October 2022; accepted 29 November 2022; published 14 December 2022)

Rare-earth doped crystals have long coherence times and the potential to provide quantum interfaces between microwave and optical photons. Such applications benefit from a high cooperativity between the spin ensemble and a microwave cavity—this motivates an increase in the rare-earth ion concentration which in turn impacts the spin coherence lifetime. We measure spin dynamics of two rare-earth spin species,  $^{145}\text{Nd}$  and  $\text{Yb}$ , doped into  $\text{Y}_2\text{SiO}_5$ , coupled to a planar microwave resonator in the high-cooperativity regime, in the temperature range 1.2 K to 14 mK. We identify relevant decoherence mechanisms, including instantaneous diffusion arising from resonant spins and temperature-dependent spectral diffusion from impurity electron and nuclear spins in the environment. We explore two methods to mitigate the effects of spectral diffusion in the  $\text{Yb}$  system in the low-temperature limit, first, using magnetic fields of up to 1 T to suppress impurity spin dynamics and, second, using transitions with low effective  $g$  factors to reduce sensitivity to such dynamics. Finally, we demonstrate how the “clock transition” present in the  $^{171}\text{Yb}$  system at zero field can be used to increase coherence times up to  $T_2 = 6(1)$  ms.

DOI: [10.1103/PhysRevB.106.245416](https://doi.org/10.1103/PhysRevB.106.245416)

### I. INTRODUCTION

Rare-earth ions (REIs) doped into yttrium orthosilicate ( $\text{Y}_2\text{SiO}_5$ , or YSO) are promising systems for use in solid-state quantum technologies. They have optical [1] and microwave [2] spin transitions with coherence times of milliseconds for electron spin resonance transitions [3–5] and hours for nuclear spin transitions [6,7]. These properties have stimulated proposals for the use of such REIs in microwave [8,9] or optical [10–12] multimode quantum memories and quantum microwave to optical transducers [13–15]. High-efficiency storage and retrieval protocols based on spins coupled to microwave resonators require cooperativity,  $C \geq 1$ , and, consequently, high spin density [16–19]. However, such high spin densities introduce spin decoherence mechanisms such as spectral [20] and instantaneous [21] diffusion, which must be understood and mitigated to achieve useful quantum memory lifetimes.

In this paper we perform pulsed electron spin resonance (ESR) measurements of two REI systems ( $^{145}\text{Nd}$  and  $^{\text{nat}}\text{Yb}$ ) in YSO, using planar superconducting resonators [22] that are strongly coupled to the spin ensemble ( $C \sim 4\text{--}245$ ). First, we measure and identify instantaneous diffusion as a limiting decoherence mechanism in highly doped spin systems.

We observe a strongly temperature-dependent coherence time and show that this is due to suppression of spectral diffusion arising from spin bath polarization at low temperatures. Nevertheless, even at a base temperature of 14 mK, coherence times are limited by spectral diffusion from electron spin subensembles. Finally, we show how so-called “clock” (or zero first-order Zeeman [23]) transitions and isotopic purification of the REI impurities can extend coherence times  $T_2$  at zero field to over 6 ms.

### II. EXPERIMENTAL AND SPIN SYSTEM

We study three  $\text{Y}_2\text{SiO}_5$  samples: one doped with (isotopically purified)  $^{145}\text{Nd}^{3+}$  ions (nuclear spin  $I = 7/2$ ) at 200 ppm ( $4 \times 10^{18} \text{ cm}^{-3}$ ), one with a natural isotopic abundance of  $\text{Yb}^{3+}$  at 50 ppm ( $1 \times 10^{18} \text{ cm}^{-3}$ ), and one with  $^{171}\text{Yb}^{3+}$  at 5 ppm ( $1 \times 10^{17} \text{ cm}^{-3}$ ). The crystals were cut along their principal dielectric axes ( $\mathbf{D}_1$ ,  $\mathbf{D}_2$ ,  $\mathbf{b}$ ) with faces perpendicular to  $\mathbf{b}$  polished for resonator fabrication. Due to its larger ionic radius,  $^{145}\text{Nd}$  preferentially substitutes Y in one of the crystal sites in  $\text{Y}_2\text{SiO}_5$ , whereas Yb equally populates both sites. The Nd sample was studied using a “thin-ring” NbN resonator [22,24] with a film thickness of 45 nm, resonant frequency  $f_c = 8.07$  GHz, and loaded quality factor  $Q \approx 72000$ . For the Yb samples we used several spiral NbN resonators [25] with a film thickness of 15 nm to explore different regimes: a resonator with  $f_c = 5.04$  GHz and  $Q \approx 31000$ , as well as lower-frequency resonators

\*joseph.alexander.18@ucl.ac.uk

†jjl.morton@ucl.ac.uk

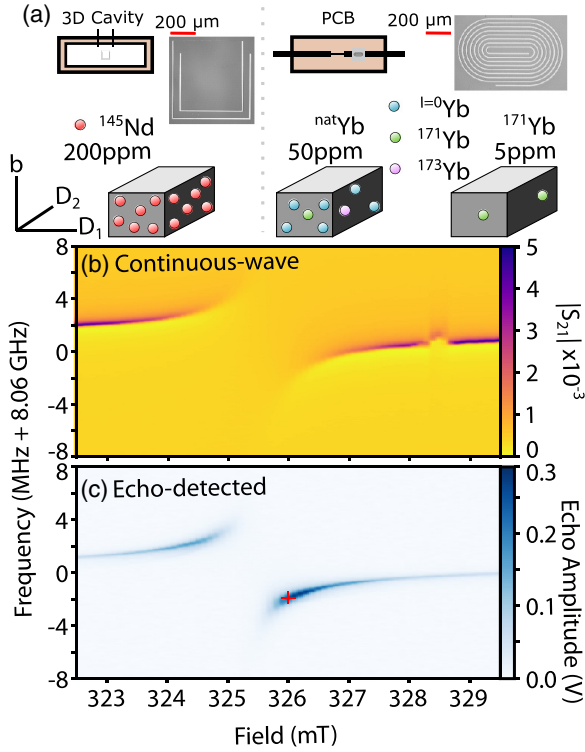


FIG. 1. (a) The three rare-earth ion doped YSO samples studied each had superconducting NbN resonators patterned on them to enable ESR studies of the spin systems. The  $^{145}\text{Nd}$  sample (200 ppm) was measured using a “thin-ring” resonator [22] and then placed inside a three-dimensional (3D) copper cavity. The Yb samples were measured using a spiral resonator and placed on top of a Printed Circuit Board designed to maximize spin signal. (b) Measurement of the  $^{145}\text{Nd}$   $m_i = +\frac{7}{2}$  transition around  $B = 326$  mT along  $D_1$ , showing the avoided crossing in a continuous-wave measurement with a vector network analyser, where the background  $S_{21}$  transmission of the 3D cavity has been subtracted for clarity. (c) Echo amplitude from a two-pulse Hahn echo sequence with the echo-detected avoided crossing. The darker blue regions indicate larger echo amplitude; these are points where there is more hybridization between the resonator and the spins. The operating point for subsequent pulsed experiments on Nd is indicated by the red cross.

targeting the zero-field clock transition with  $f_c = 2.372$  GHz and  $Q \approx 26000$ . The spiral resonator design was better suited to the lower target microwave frequencies for Yb, while maintaining a footprint of about  $500 \times 800 \mu\text{m}^2$ . All samples were measured using a dilution refrigerator (base temperature of  $\sim 14$  mK) with a (3-1-1) T vector magnet. The Nd sample was mounted on a sapphire platform inside a copper box, while the Yb samples were mounted over a copper strip line designed with impedance steps for efficient collection of signal as outlined in the Supplemental Material (SM) [26]. An overview of all three systems is shown in Fig. 1(a).

Spin transitions were located by monitoring  $S_{21}(f)$  while sweeping applied magnetic field and identifying avoided crossings between the resonator and electron spin ensemble, as shown for Nd in Fig. 1(b). A similar measurement is possible using pulsed ESR by monitoring the two-pulse Hahn echo as a function of both magnetic field and frequency, as shown

in Fig. 1(c). The maximum echo intensity is measured at  $B = 326$  mT, where the resonator and spin line hybridize; we also note the weak background echo which can be measured far from the spin line (see the SM [26]). Fitting this avoided crossing and extracting the ensemble coupling strength  $g_{\text{ens}}$ , spin linewidth  $\gamma_s$ , and resonator linewidth  $\kappa_c$  [27] return cooperativity  $C = g_{\text{ens}}^2 / \gamma_s \kappa_c = 245$  with  $g_{\text{ens}} > \kappa_c, \gamma_s$ , showing the system is in the strong-coupling regime, well suited for high-efficiency memories.

The Nd and Yb impurities studied here are well described by the spin Hamiltonian:

$$\mathcal{H} = \mathbf{S} \cdot \hat{\mathbf{A}} \cdot \mathbf{I} + \mu_B \mathbf{B} \cdot \hat{\mathbf{g}} \cdot \mathbf{S} - \mu_n \mathbf{B} \cdot g_n \cdot \mathbf{I}, \quad (1)$$

where the electron spin  $\mathbf{S}$  interacts with the nuclear spin  $\mathbf{I}$  described by a hyperfine tensor  $\hat{\mathbf{A}}$  and to an external magnetic field  $\mathbf{B}$  via a  $g$  tensor  $\hat{\mathbf{g}}$ . The nuclear spin also interacts with the field via a nuclear  $g$  factor  $g_n$ , the values of which are given in the SM [26]. The large anisotropy of the electron  $g$  tensor results in an ESR spectrum which has a strong angular dependence and allows for regimes in which dipole coupling between rare-earth spins can be suppressed [28].

### III. SPIN DECOHERENCE MECHANISMS

#### A. Instantaneous diffusion

A common decoherence mechanism in bulk doped spin systems [29]—particularly relevant in samples that are highly doped to achieve strong coupling to resonators—arises from the dipolar interaction between resonant spins [21,30]. Such interactions are not refocused in a two-pulse Hahn echo (because both interacting spins are flipped), leading to a decoherence mechanism known as *instantaneous diffusion* (ID), whose rate is proportional to  $n$ , the density of resonant spins, as [30,31]

$$T_2(\text{ID}) = \frac{9\sqrt{3}\hbar}{\pi\mu_0(g\mu_B)^2n}. \quad (2)$$

Here,  $g$  is the effective  $g$  factor, while  $h$ ,  $\mu_0$ , and  $\mu_B$  are Planck’s constant, the vacuum permeability, and the Bohr magneton, respectively.

We use two approaches to study the effect of resonant spin density on coherence time: (i) exploiting differences in the natural abundance of those Yb isotopes which can be spectrally separated due to their nuclear spin and (ii) using the variation of spin density across the inhomogeneously broadened ESR transition. The resonant spin density can be estimated based on the product of the impurity concentration of Yb, the natural abundance of the relevant isotope(s), the two occupied sites in YSO, and the fraction of spins which are addressed given a particular excitation/resonator bandwidth. For example, here, a bandwidth of about 66 kHz is set by the microwave  $\pi$ -pulse length of  $15 \mu\text{s}$ , which should be compared to the inhomogeneously broadened spin linewidth of  $\gamma_s/2\pi = 8.7$  MHz. This is explained in full in Sec. V of the SM [26].

In Fig. 2 we show echo-detected magnetic field sweeps across two ESR transitions: one arising from the set of Yb

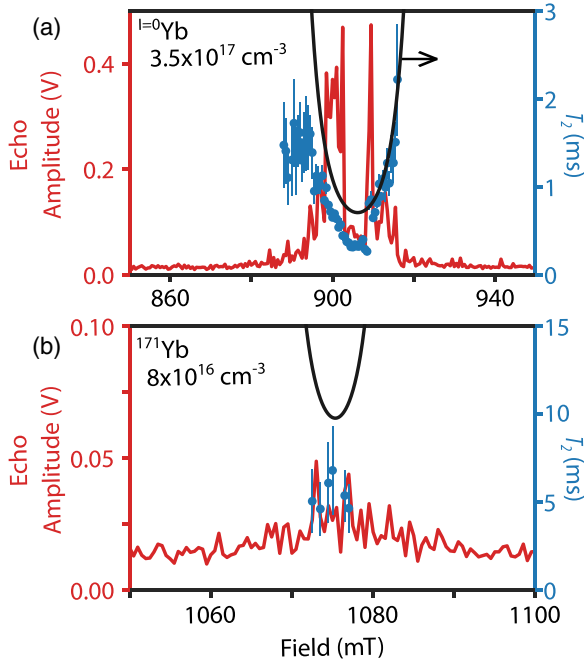


FIG. 2. Echo-detected field sweep of  $^{\text{nat}}\text{Yb}$  at high field (red curves). The (a)  $I=0\text{Yb}$  and (b)  $^{171}\text{Yb}$  ESR lines can be separately studied at 905 and 1075 mT, respectively. The effect of ID can be observed as  $T_2$  (blue data points) is measured across the ESR line. For  $I=0\text{Yb}$ , the coherence time decreases significantly at the center of the spin line, where the density of resonant spins is maximal. In both panels, the black curve is the calculated ID limit on  $T_2$  using Eq. (2) with no fitting parameters (see main text).

isotopes with nuclear spin  $I = 0$  (17.5 ppm) and the other arising from  $^{171}\text{Yb}$  (3.5 ppm). The resonator frequency shifts as the spin transition is approached [as illustrated for Nd in Fig. 1(c)], so the applied microwave frequency is adjusted at each magnetic field value to follow the resonator. The drop in echo amplitude seen in the center of the line in Fig. 2(a) arises from the strong resonator/spin hybridization and is not a result of a distortion of the ESR line shape, which we assume here to follow a simple Gaussian profile. We measure  $T_2$  across the inhomogeneously broadened ESR line shape and observe a drop in the coherence time at the center, where the resonant spin density is greatest. Indeed, using the nominal 50 ppm concentration of  $\text{Yb}^{3+}$ , natural isotopic abundance, expected excitation bandwidth, and measured ESR linewidth with Eq. (2), we can accurately reproduce the observed  $T_2$  values with no free parameters. Towards the tails of the ESR line, where the resonant spin density is lowest, the measured  $T_2$  begins to deviate from that limited by ID and saturates at 1–2 ms. Performing the same measurement for the  $^{171}\text{Yb}$  transition, we observe no change in  $T_2$  over the ESR line shape—this is expected because we can use the results above to predict an ID-limited  $T_2$  of 11 ms (thanks to the lower spin concentration of  $^{171}\text{Yb}$ ), which is well above the measured values of 6(2) ms. We therefore confirm that ID is not a limiting decoherence mechanism in the  $^{171}\text{Yb}$  system for this sample and move on to explore alternative mechanisms.

## B. Spectral diffusion

### 1. Temperature dependence

Cross-relaxation processes (or spin flip-flops) between spins cause the local magnetic environment to fluctuate over time, giving rise to *spectral diffusion* [20,30,32]. Reducing the temperature of the spin bath polarizes it, reducing the rate of flip-flops and, consequently, the effects of spectral diffusion [33–35]. Figure 3 shows such an increase in coherence time with decreasing temperature for both the  $^{145}\text{Nd}$  and  $^{\text{nat}}\text{Yb}$  samples: in Nd from 24(1)  $\mu\text{s}$  at 1.2 K to 0.41(1) ms at 14 mK and in  $^{\text{nat}}\text{Yb}$  increasing from 33(7)  $\mu\text{s}$  to 3.4(1) ms over the same temperature range. As in Ref. [9], we model the temperature dependence of  $T_2$  assuming that spectral diffusion is caused by one or more subensembles of spins with distinct resonant frequencies. In our  $^{145}\text{Nd}$  sample, the different projections of the  $I = 7/2$  nuclear spin along the applied magnetic field form the dominant contribution to such subensembles, while in the  $^{\text{nat}}\text{Yb}$  sample, multiple isotopes with different nuclear spins and the projections of nuclear spin for  $I > 0$  act as subensembles.

We can write the decoherence rate  $\Gamma = 1/T_2$  of the “central spin” being studied as [20,32]

$$\Gamma = \frac{R\Gamma_{\text{SD}}}{2} \left( \sqrt{\Gamma_0^2 + \frac{R\Gamma_{\text{SD}}}{\pi}} - \Gamma_0 \right)^{-1} \approx \frac{\sqrt{\pi R\Gamma_{\text{SD}}}}{2}, \quad (3)$$

where  $R$  is the spin flip rate,  $\Gamma_{\text{SD}}$  is the spectral diffusion linewidth, and  $\Gamma_0$  is a residual decoherence rate in the absence of spectral diffusion. When the dominant noise process is spectral diffusion (i.e.,  $\Gamma_0 \ll \sqrt{R\Gamma_{\text{SD}}}$ ), we neglect the  $\Gamma_0$  dependence of  $T_2$ . Assuming that spectral diffusion occurs from spin flips due to spin-spin interactions between resonant subensembles, we can write the flip-flop rate within the  $i$ th subensemble of spins as [28]

$$R_i = \beta_{\text{ff}}(\theta) \frac{n_i^2}{\Gamma_i} \text{sech}^2 \left( \frac{T_{Z,i}}{T} \right), \quad (4)$$

where  $n_i$  and  $\Gamma_i$  are, respectively, the spin density and linewidth of the  $i$ th subensemble and  $\beta_{\text{ff}}$  is a parameter which encompasses the angular dependence of the coupling parameter and the  $g$  tensor.  $T_{Z,i}$  is the Zeeman temperature for each subensemble:  $T_{Z,i} = hf/k_B$ , where  $f$  is the transition frequency. In the case of an isotropic medium  $\beta_{\text{ff}} \propto \mu_B^4 g^4$ , however, this does not hold in the case of strong anisotropy, as in YSO [3,36–38]. This term is proportional to the rate derived from Fermi’s golden rule, taking the dipole coupling as a perturbation of the spin Hamiltonian. To account for this we rewrite  $\beta_{\text{ff}} = \xi \frac{\mu_B^4 \mu_0^2}{h^2} M_i^2$ , where  $M_i$  is the matrix element of each subensemble transition and  $\xi$  is a coupling rate fit parameter. We thus rewrite  $R$  as

$$R = \xi \frac{\mu_B^4 \mu_0^2}{h^2} M_i^2 \frac{n_i^2}{\Gamma_i} \text{sech}^2 \left( \frac{T_{Z,i}}{T} \right). \quad (5)$$

The spectral diffusion linewidth of the  $i$ th subensemble (the frequency shift of the central spin by the spins in this subensemble due to dipolar interactions) is given by [20]

$$\Gamma_{\text{SD},i} = \frac{\pi \mu_0 \mu_B^2}{9\sqrt{3}h} n_i g_i g \text{sech}^2 \left( \frac{T_{Z,i}}{T} \right), \quad (6)$$

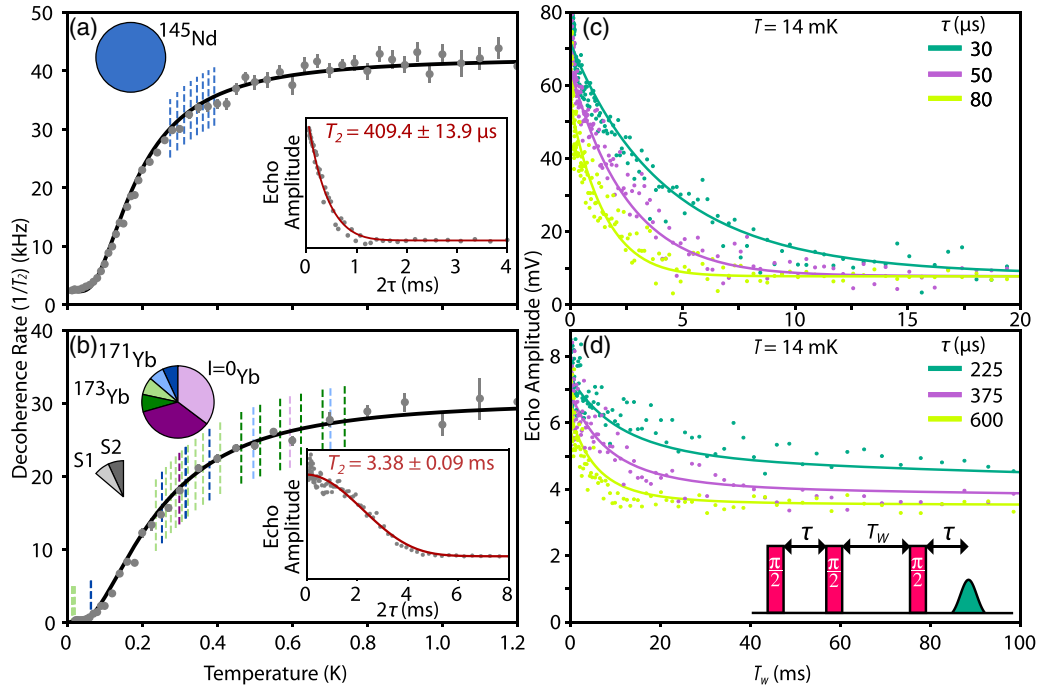


FIG. 3. The decoherence rate  $1/T_2(T)$  measured from 1.2 K to 14 mK for (a) the  $^{145}\text{Nd}$  sample and (b) the  $^{\text{nat}}\text{Yb}$  sample. In both samples, the decoherence rate drops with temperature due to suppression of spectral diffusion below the Zeeman temperature of various spin subensembles present in the sample. The solid curve is a fit using Eq. (7), and dashed lines indicate the Zeeman temperatures of all the subensembles used in the fit, whose relative abundance is shown in pie charts. The insets in (a) and (b) show the measurement of  $T_2$  at the lowest temperature, 14 mK, using a two-pulse echo sequence. (c) and (d) Stimulated (three-pulse) echo decays for the  $^{145}\text{Nd}$  and  $^{\text{nat}}\text{Yb}$  samples, respectively, aiming to determine the source of decoherence at the base temperature of 14 mK. The values of  $\tau$  in the three-pulse echo sequence were chosen for each sample in proportion with  $T_2$  at 14 mK. For  $^{\text{nat}}\text{Yb}$  ( $^{145}\text{Nd}$ ), the magnetic field was 370 mT (326 mT), and microwave frequency was 5.04 (8.07) GHz.

where  $g$  and  $g_i$  are the effective  $g$  factors of the central and  $i$ th spins, respectively. Combining Eqs. (3)–(6) gives an expression for the overall temperature-dependent decoherence rate, where the spectral diffusion component contains contributions from multiple subensembles, similar in form to that given in Ref. [9]:

$$\Gamma(T) = \Gamma_{\text{res}} + \sqrt{\frac{\pi \mu_0^3 \mu_B^6}{9 \sqrt{3} h^3 \Gamma}} g \sum_i \frac{\sqrt{\xi} n_i^{3/2} M_i}{\left(1 + e^{\frac{T_{Z,i}}{T}}\right) \left(1 + e^{-\frac{T_{Z,i}}{T}}\right)}. \quad (7)$$

$\Gamma_{\text{res}}$ , which we treat as a fit parameter, is a temperature-independent decoherence rate due to, for example, spectral diffusion from spins that remain unpolarized even at our base temperature of 14 mK.  $\xi$  is a single temperature-independent fit parameter reflecting the average effective  $g$  factor  $g_i$  of all subensembles.  $M_i$  was calculated using EASYSYSPIN [39]. We assume the linewidth of each subensembles is equal to that of the central spin. The relative populations of the ground  $P_{\downarrow}$  and excited  $P_{\uparrow}$  states involved in the flip-flop processes for each subensemble are  $P_{\downarrow} = [1 + \exp(+T_{Z,i}^i/T)]^{-1}$  and  $P_{\uparrow} = [1 + \exp(-T_{Z,i}^i/T)]^{-1}$  according to Boltzmann statistics [9,34].

Fits to Eq. (7), where  $\xi$  and  $\Gamma_{\text{res}}$  are the only free parameters, are shown in Fig. 3. The resulting free parameter  $\xi$  returns values of 1.94(1) for Nd and 12(1) for Yb. As  $\xi \propto g^4$ , the difference in these values is attributed to the differences in the  $g$ -tensor components, in particular  $g_z = 4.17$  in Nd,

whereas  $g_z = 6.06$  in Yb site 2 [3,37]. Notably, the Nd sample also has a substantially larger residual decoherence rate  $\Gamma_{\text{res}}$  at the base temperature of the dilution fridge than the Yb sample; however, we believe this is partially due to poor thermalization in the Nd sample, as outlined in the SM [26].

## 2. Low-temperature limit

To further investigate the residual decoherence mechanism present at low temperatures, we used a three-pulse stimulated echo sequence ( $\frac{\pi}{2}$ - $\tau$ - $\frac{\pi}{2}$ - $T_w$ - $\frac{\pi}{2}$ - $\tau$ -echo) [32] to directly measure the component due to spectral diffusion. The inhomogeneous fields induced by planar resonators on bulk doped crystals means that the pulses are not true  $\frac{\pi}{2}$  pulses. The stimulated echo amplitude is given by [32]

$$A(\tau, T_w) = A_0 \exp \left[ - \left( \frac{T_w}{T_1} + 2\pi \tau \Gamma_{\text{eff}} \right) \right], \quad (8)$$

where  $A_0$  is a fitted amplitude,  $\tau$  and  $T_w$  are delay parameters used in the pulse sequence, and  $T_1$  is the spin relaxation time, measured to be 696 ms (Nd) and 47 ms (Yb) from data shown in the SM [26] (see also Refs. [40,41] therein). The effective decoherence rate  $\Gamma_{\text{eff}}$  is

$$\Gamma_{\text{eff}} = \Gamma_0 + \frac{1}{2} \Gamma_{\text{SD}} (R\tau + 1 - e^{-R\tau}), \quad (9)$$

where  $\Gamma_{\text{SD}}$  is the spectral diffusion linewidth,  $R$  is the total spin-flip rate, and  $\Gamma_0$  is a residual decoherence rate. As the



duration of the experiment is much shorter than the measured  $T_1$  (see Sec. VII in the SM [26]), we assume all decoherence occurs from spectral diffusion and set  $\Gamma_0 = 0$ . Figures 3(c) and 3(d) show the three-pulse echo decay as  $T_W$  is increased for three different values of  $\tau$ . As  $T_2$  is longer for the  $^{171}\text{Yb}$  sample, longer  $\tau$  values were chosen so that both samples investigate the same  $\tau/T_2$  ratio.

As shown in the SM, fitting Eqs. (8) and (9) to the data in Figs. 3(c) and 3(d) does not uniquely determine  $R$  and  $\Gamma_{SD}$  due to their covariance; however, the fit routine does reliably determine their product. In Nd these fits return  $R\Gamma_{SD} = 3.5(4) \times 10^6 \text{ Hz}^2$ , which allows us to extract a limit on the coherence time using Eq. (3) of  $T_2 = 0.60(3) \text{ ms}$ . Using Eqs. (4) and (6) with the stimulated echo fit, an estimated spin bath temperature of 61 mK is obtained (significantly higher than the measured base temperature). Further evidence of the poor thermalization is seen in the deviation from the expected temperature dependence of the echo magnitude below about 100 mK (see the SM).

Following a similar analysis for the Yb sample, the fits return  $R\Gamma_{SD} = 1.3(3) \times 10^5 \text{ Hz}^2$ . This results in a spectral diffusion limited  $T_2$  of 3.1(7) ms, consistent with the two-pulse echo value of 3.38(9) ms, and an estimated spin bath temperature of 38 mK. We explore the source of spectral diffusion in the Yb sample and compute the effect of  $^{89}\text{Y}$  nuclear flip-flops. Following the methods presented in Ref. [20], described further in the SM, we calculate a spectral diffusion rate and linewidth from  $^{89}\text{Y}$  flip-flops:  $R_Y\Gamma_{SD,Y} = 1.05 \times 10^5 \text{ Hz}^2$  with a limiting  $T_2 = 3.48 \text{ ms}$ . This is in agreement with  $T_2$  measured with a two-pulse echo, and we therefore conclude that the low-temperature coherence time is limited by  $^{89}\text{Y}$  nuclear spin flip-flops.

#### IV. MITIGATING SPIN DECOHERENCE

In Sec. III we found the coherence of  $^{171}\text{Yb}$  electron spins in  $^{\text{nat}}\text{Yb}$ -doped YSO at 14 mK to be primarily limited by spectral diffusion from  $^{89}\text{Y}$  nuclear spin flip-flops when measured at 5.04 GHz and 370 mT. We next explore two strategies to further suppress spin decoherence: first, exploiting the substantial anisotropy of the  $g$  tensor and rotating the magnetic field to orientations which give the lowest effective  $g$  factor and, second, exploring the clock transition at zero magnetic field for which the first-order sensitivity of the ESR transition frequency goes to zero with respect to the magnetic field.

##### A. Increasing magnetic field

For a given ESR transition frequency, the magnetic field orientation at which the effective  $g$  factor is lowest is that which provides the ESR resonance at the maximum magnetic field. We investigate this approach for  $^{171}\text{Yb}$  using a lower resonator frequency (2.43 GHz) than that used above so that the resonant fields remain within the range of our vector magnet. As the magnetic field is rotated in the  $D_1$ - $D_2$  plane, the resonant field reaches a peak of 1.2 T; however, due to experimental limitations the highest field we studied was 1.07 T, at an angle of  $-131^\circ$  from  $D_1$ . Figure 4(a) shows how  $T_2$  varies as the field is rotated in the  $D_1$ - $D_2$  plane. Due

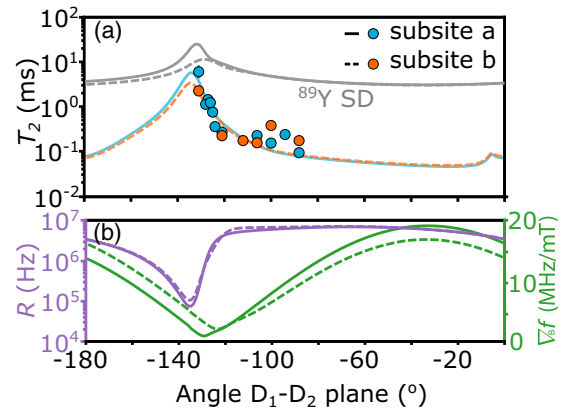


FIG. 4. Angular dependence of  $T_2$  in the high-field regime. (a) The measured coherence time of  $^{171}\text{Yb}$  as the applied field is rotated in the  $D_1$ - $D_2$  plane; the subsite degeneracy is lifted due to a slight misalignment with the  $b$  axis. At  $-131^\circ$ ,  $T_2$  reaches a maximum, which corresponds well with the modeled coherence time (dashed lines) extracted using  $R\Gamma_{SD}$ . The gray curves correspond to the predicted coherence time in the absence of electron spin spectral diffusion. (b) As the angle of the applied field is rotated in the  $D_1$ - $D_2$  crystal plane, the anisotropic  $g$  tensor results in an angular dependence of the spectral diffusion rate  $R$  and  $^{171}\text{Yb}$ 's sensitivity to it  $\nabla f$ . At angles of about  $131^\circ$ , both  $R$  and  $\nabla f$  reach a minimum, resulting in an increase in the coherence time.

to a small misalignment towards the  $b$  axis (estimated to be  $< 0.8^\circ$ ), the degeneracy of the two crystal subsites is lifted.

Considering first the coherence times measured at an angle of around  $-88^\circ$  from  $D_1$  (approximately along  $D_2$ ), we see that they fall substantially below that predicted due to  $^{89}\text{Y}$  nuclear spin flip-flops. Here, the magnetic field was 154 – 174 mT, less than half that used in Sec. III due to the lower resonator frequency. In this regime, therefore, some electron spin subensembles appear to remain unpolarized at 14 mK and contribute to spectral diffusion. As the magnetic field orientation rotates further away from  $D_1$ , the effective  $g$  factor decreases, demanding a larger magnetic field magnitude to satisfy the resonance condition for  $^{171}\text{Yb}$ —this increased magnetic field in turn serves to further polarize electron spin subensembles in the bulk, as was achieved in Sec. III by lowering temperature. Therefore, approaching the optimum field orientation of  $-133^\circ$  offers the twin benefits of reducing magnetic field noise by polarizing the bath at high field (minimizing  $R\Gamma_{SD}$ ) while also reducing the sensitivity  $\nabla_B f$  of the central spin to that noise. Indeed, at  $-131^\circ$ , the coherence time of subsite  $a$  was measured to be 6(2) ms. Both  $\nabla_B f$  and  $R\Gamma_{SD}$  are plotted in Fig. 4(b), based on the relationships in Eqs. (4) and (6) and the spin Hamiltonian (see Sec. XI in the SM for further details [26]). The resulting model for  $T_2$  follows the observed data well, including the different times seen for the two subsites. Figure 4(a) also shows the simulated impact of spectral diffusion from  $^{89}\text{Y}$  nuclear spins varies in this regime. We can therefore predict that if the 5.04 GHz resonator were used in this experiment, we would expect a  $T_2$  of 25.5 ms (similar to that measured in [5]) at  $-132.7^\circ$ ; however, this would occur at 3.07 T, beyond the capabilities of our experimental setup.

### B. Around zero magnetic field

We showed above that using large magnetic fields (around 1 T) applied at specific orientations can extend the  $^{171}\text{Yb}$  electron spin  $T_2$  to several milliseconds. However, such fields introduce practical challenges when embedding  $^{171}\text{Yb}$  within more complex superconducting circuits, and indeed, to integrate with superconducting qubits it is desirable to operate close to zero magnetic field. One of the attractive features of  $^{171}\text{Yb}$  as a quantum memory is the clock transition it exhibits at zero field—here, the sensitivity to magnetic field noise goes to zero, to first order, which should reduce the impact of spectral diffusion on the spin coherence time. The use of a microresonator to perform ESR at a clock transition at zero magnetic field requires precise control of its resonance frequency to match the  $^{171}\text{Yb}$  zero-field splitting of 2.370 GHz. This challenge is made more acute by the narrowing of the ESR linewidth which occurs around the clock transition. We explore ESR in the low-field regime of  $^{\text{nat}}\text{Yb}$  doped YSO using a resonator with a frequency within 2 MHz of the clock transition (comparable to the spin-resonator coupling strength).

To investigate the impact of the clock transition on spin coherence, we perform magnetic field sweeps along a fixed direction of  $49^\circ$  in the  $D_1$ - $D_2$  plane—at this field orientation  $\nabla_B f$  follows a local minimum, leading to the longest expected coherence times (see the SM). Figure 5(a) shows how  $T_2$  increases sharply as the field passes through zero, reaching a maximum of 1.77(6) ms at 0 mT. While a strong increase in coherence time (over an order of magnitude) is observed around zero field compared to fields up to 40 mT at this orientation, the increase remains well below that predicted by the decrease in sensitivity to magnetic field noise  $\nabla_B f$ . Indeed, the times measured here at the nominal clock transition at zero field remain several times shorter than those measured at high fields ( $\sim 1$  T) described above where the effective  $g$  factor drops to 0.1. We attribute this behavior to the impact of environmental electron spins that not only are unpolarized but also become mutually resonant at zero magnetic field, leading to a large increase in the effective magnetic field noise. In this  $^{\text{nat}}\text{Yb}$  sample, isotopes with zero nuclear spin ( $^{170}\text{Yb}$ ) comprise approximately 70% of the natural abundance of Yb impurities, providing a large bath of unpolarized electron spins. Approaching zero magnetic field, we conclude that the rate of spectral diffusion increases faster than  $\nabla_B f$  of  $^{171}\text{Yb}$  decreases, limiting the enhancement of  $T_2$  (see Sec. XII of the SM for more details [26]).

### C. Isotopic purification of Yb

When seeking to exploit  $^{171}\text{Yb}$  defect spins in YSO as a candidate quantum memory medium, any other isotopes of Yb present in the bulk serve only to introduce additional sources of decoherence, particularly at the low magnetic fields used to access the clock transition. We next explore the use of isotopically pure  $^{171}\text{Yb}$  doped  $\text{Y}_2\text{SiO}_5$ , using a resonator design identical to that used in the  $^{\text{nat}}\text{Yb}$  sample with a resonant frequency of 2.368 GHz. Figure 5(b) plots measured  $T_2$  as a function of magnetic field along the same  $49^\circ$  orientation as above (the lower resonator frequency here limited the addressable field range). In the absence of other Yb isotopes the

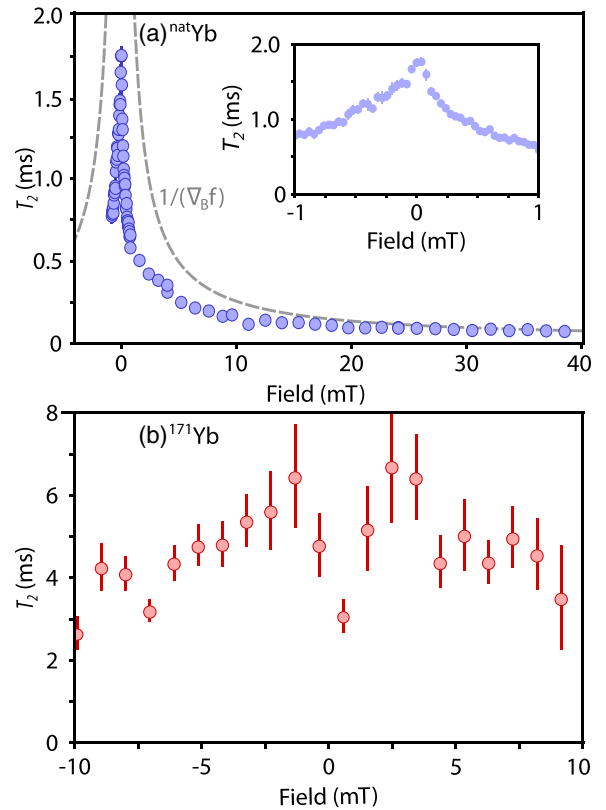


FIG. 5. Field dependence of the coherence time of  $^{171}\text{Yb}$  at low field for both (a) the  $^{\text{nat}}\text{Yb}$  doped and (b) isotopically pure  $^{171}\text{Yb}$  doped systems. While  $T_2$  increases substantially [to 1.77(6) ms] as the field approaches zero (highlighted by the inset, which is zoomed in around zero magnetic field) in the  $^{\text{nat}}\text{Yb}$  system, the coherence time is not as long as that measured at high field [6(2) ms]. The coherence time deviates from the trend in decreasing  $\nabla_B f$ , as shown by the gray dashed line. This is due to the presence of an unpolarized spin bath of other Yb isotopes at zero field, which is highlighted by the increased coherence in the isotopically pure  $^{171}\text{Yb}$  system in (b). Here, a longer maximum  $T_2$  is measured [6(2) ms], and a wider region of long coherence is also observed.

coherence times are now over an order of magnitude longer in this field range of 0–10 mT, reaching a gentle maximum of 6(1) ms at 2.5 mT—the longest  $^{171}\text{Yb}$   $T_2$  measured in all the systems we studied here. As the field magnitude reaches  $< 1$  mT, the measured  $T_2$  shortens, which we attribute to the impact of  $^{89}\text{Y}$  nuclear spins at low magnetic field. The coherence decay curves themselves exhibit electron spin echo envelope modulation (ESEEM), which occurs when the electron spin interacts with one or more neighboring nuclear spins and the coherent quantum state is transferred between the two. As the frequency of these oscillations is proportional to the Larmor frequency, the revival of the electron spin echo goes to infinity as the field goes to zero. This means that a coherence curve cannot be fitted to the echo decay, so this appears as a decrease in  $T_2$ ; this is a problem present in all systems with a strong hyperfine interaction [42]. Another possibility for the dip in coherence at 0 mT is the changing behavior of the nuclear spin bath around the clock transition [43]; here, the  $^{89}\text{Y}$  nuclear spins are no longer in the frozen core, so there

is an increase in spectral diffusion. This interaction between the electron spin and the  $^{89}\text{Y}$  nuclear spins is a general issue for operating quantum memory at zero field which effects all rare earths doped in  $\text{Y}_2\text{SiO}_5$ , motivating studies in other host materials with lower nuclear spin concentrations [44,45].

## V. CONCLUSION

We used on-chip superconducting resonators to perform pulsed ESR measurements on  $^{145}\text{Nd}$  and  $^{171}\text{Yb}$  in YSO in the high-cooperativity regime  $C = 4$  to 245. Cooling the spin ensemble down to a nominal base temperature of 14 mK was shown to extend coherence times by polarizing the bath of electron spins in the environment, leading to  $T_2 = 0.41(1)$  ms for  $^{145}\text{Nd}$  (likely limited by poor sample thermalization) and  $T_2 = 3.38(9)$  ms for  $^{171}\text{Yb}$ , believed to be limited by spectral diffusion from  $^{89}\text{Y}$  nuclear spins in the host. We explored two routes to suppressing spectral diffusion in  $^{171}\text{Yb}$ . The first involved rotating the applied magnetic field to access transitions with a low effective  $g$  factor to enable the coherence time of 6(2) ms. The high magnetic field ( $> 1$  T) serves to polarize the spin bath, reducing the spectral diffusion rate, while the low effective  $g$  factor reduces the sensitivity to spectral diffusion, so the coherence time is further increased. Second, we studied coherence times around the clock transition, showing that the strong reduction in sensitivity of magnetic field noise around zero field is somewhat compensated by a large increase in magnetic field noise from spin flip-flops from other Yb isotopes. Using an isotopically pure  $^{171}\text{Yb}:\text{YSO}$  sample, we were able to increase  $T_2$  to a maximum of 6(1) ms.

Overall, based on the understanding we have obtained on decoherence mechanisms in these system, we conclude that  $^{171}\text{Yb}$  offers clear advantages over  $^{145}\text{Nd}$  for spin-based

memories in YSO arising from its lower nuclear spin ( $I = 1/2$ ) and thus reduced concentration of nonresonant electron spin in the environment. The longest coherence times for  $^{171}\text{Yb}$  are predicted to be achieved at higher magnetic fields (e.g., 25 ms at fields of about 3 T), although these show limited compatibility with superconducting circuits in general. ESEEM from  $^{89}\text{Y}$  is likely to pose a limiting factor in the use of  $^{171}\text{Yb}$  spins at zero magnetic field; however, this could be avoided by moving to other crystalline hosts, such as  $\text{CaWO}_4$  [5]. Quantum memory schemes typically require high-fidelity control of the spins, which is challenging for bulk-doped rare-earth ion spins such as those studied here—spatially confining such spins is therefore likely to be advantageous, for example, through implantation or lithography.

## ACKNOWLEDGMENTS

This work has received funding from the U.K. Engineering and Physical Sciences Research Council (EPSRC) through the Centre for Doctoral Training in Delivering Quantum Technologies (Grant No. EP/L015242/1), QUES2T (Grant No. EP/N015118/1), and the Skills Hub in Quantum Systems Engineering: Innovation in Quantum Business, Applications, Technology and Engineering (InQuBATE), Grant No. EP/P510270/1, as well as from the European Research Council (ERC) via LOQOMOTIONS (H2020- EU.1.1., Grant No. 771493). We would like to acknowledge support from the U.K. Department for Business Energy and Industrial Strategy (BEIS) through the U.K. National Quantum Technologies Programme and the ANR MIRESPIN project, Grant No. ANR-19-CE47-0011 of the French Agence Nationale de la Recherche and DGA.

- 
- [1] C. Thiel, T. Böttger, and R. Cone, Rare-earth-doped materials for applications in quantum information storage and signal processing, *J. Lumin.* **131**, 353 (2011).
- [2] A. Ortu, A. Tiranov, S. Welinski, F. Fröwis, N. Gisin, A. Ferrier, P. Goldner, and M. Afzelius, Simultaneous coherence enhancement of optical and microwave transitions in solid-state electronic spins, *Nat. Mater.* **17**, 671 (2018).
- [3] G. Wolfowicz, H. Maier-Flaig, R. Marino, A. Ferrier, H. Vezin, J. J. L. Morton, and P. Goldner, Coherent Storage of Microwave Excitations in Rare-Earth Nuclear Spins, *Phys. Rev. Lett.* **114**, 170503 (2015).
- [4] P.-Y. Li, C. Liu, Z.-Q. Zhou, X. Liu, T. Tu, T.-S. Yang, Z.-F. Li, Y. Ma, J. Hu, P.-J. Liang, X. Li, J.-Y. Huang, T.-X. Zhu, C.-F. Li, and G.-C. Guo, Hyperfine Structure and Coherent Dynamics of Rare-Earth Spins Explored with Electron-Nuclear Double Resonance at Subkelvin Temperatures, *Phys. Rev. Appl.* **13**, 024080 (2020).
- [5] M. L. Dantec, M. Rančić, S. Lin, E. Billaud, V. Ranjan, D. Flanigan, S. Bertaina, T. Chanière, P. Goldner, A. Erb, R. B. Liu, D. Estève, D. Vion, E. Flurin, and P. Bertet, Twenty-three-millisecond electron spin coherence of erbium ions in a natural-abundance crystal, *Sci. Adv.* **7**, eabj9786 (2021).
- [6] M. Zhong, M. P. Hedges, R. L. Ahlefeldt, J. G. Bartholomew, S. E. Beavan, S. M. Wittig, J. J. Longdell, and M. J. Sellars, Optically addressable nuclear spins in a solid with a six-hour coherence time, *Nature (London)* **517**, 177 (2015).
- [7] Coherence time of over a second in a telecom-compatible quantum memory storage material, *Nat. Phys.* **14**, 50 (2017).
- [8] N. Sangouard, C. Simon, H. de Riedmatten, and N. Gisin, Quantum repeaters based on atomic ensembles and linear optics, *Rev. Mod. Phys.* **83**, 33 (2011).
- [9] S. Probst, H. Rotzinger, A. V. Ustinov, and P. A. Bushev, Microwave multimode memory with an erbium spin ensemble, *Phys. Rev. B* **92**, 014421 (2015).
- [10] T. Zhong, J. M. Kindem, J. G. Bartholomew, J. Rochman, I. Craiciu, E. Miyazono, M. Bettinelli, E. Cavalli, V. Verma, S. W. Nam, F. Marsili, M. D. Shaw, A. D. Beyer, and A. Faraon, Nanophotonic rare-earth quantum memory with optically controlled retrieval, *Science* **357**, 1392 (2017).
- [11] C. Laplane, P. Jobez, J. Etesse, N. Gisin, and M. Afzelius, Multimode and Long-Lived Quantum Correlations Between Photons and Spins in a Crystal, *Phys. Rev. Lett.* **118**, 210501 (2017).
- [12] A. Ruskuc, C.-J. Wu, J. Rochman, J. Choi, and A. Faraon, Nuclear spin-wave quantum register for a solid-state qubit, *Nature (London)* **602**, 408 (2022).
- [13] L. A. Williamson, Y.-H. Chen, and J. J. Longdell, Magneto-Optic Modulator with Unit Quantum Efficiency, *Phys. Rev. Lett.* **113**, 203601 (2014).

- [14] X. Fernandez-Gonzalvo, Y.-H. Chen, C. Yin, S. Rogge, and J. J. Longdell, Coherent frequency up-conversion of microwaves to the optical telecommunications band in an Er:YSO crystal, *Phys. Rev. A* **92**, 062313 (2015).
- [15] J. G. Bartholomew, J. Rochman, T. Xie, J. M. Kindem, A. Ruskuc, I. Craiciu, M. Lei, and A. Faraon, On-chip coherent microwave-to-optical transduction mediated by ytterbium in YVO<sub>4</sub>, *Nat. Commun.* **11**, 3266 (2020).
- [16] M. Tavis and F. W. Cummings, Exact solution for an *N*-molecule-radiation-field Hamiltonian, *Phys. Rev.* **170**, 379 (1968).
- [17] M. Afzelius, N. Sangouard, G. Johansson, M. Staudt, and C. Wilson, Proposal for a coherent quantum memory for propagating microwave photons, *New J. Phys.* **15**, 065008 (2013).
- [18] B. Julsgaard, C. Grezes, P. Bertet, and K. Mølmer, Quantum Memory for Microwave Photons in an Inhomogeneously Broadened Spin Ensemble, *Phys. Rev. Lett.* **110**, 250503 (2013).
- [19] C. Grezes, Y. Kubo, B. Julsgaard, T. Umeda, J. Isoya, H. Sumiya, H. Abe, S. Onoda, T. Ohshima, K. Nakamura, I. Diniz, A. Auffeves, V. Jacques, J.-F. Roch, D. Vion, D. Esteve, K. Moelmer, and P. Bertet, Towards a spin-ensemble quantum memory for superconducting qubits, *C. R. Phys.* **17**, 693 (2016).
- [20] T. Böttger, C. W. Thiel, Y. Sun, and R. L. Cone, Optical decoherence and spectral diffusion at 1.5 μm in Er<sup>3+</sup>: Y<sub>2</sub>SiO<sub>5</sub> versus magnetic field, temperature, and Er<sup>3+</sup> concentration, *Phys. Rev. B* **73**, 075101 (2006).
- [21] K. Salikhov, S. Dzuba, and A. Raitisimring, The theory of electron spin-echo signal decay resulting from dipole-dipole interactions between paramagnetic centers in solids, *J. Magnetic Resonance* (1969) **42**, 255 (1981).
- [22] G. Dold, C. W. Zollitsch, J. O'Sullivan, S. Welinski, A. Ferrier, P. Goldner, S. E. de Graaf, T. Lindström, and J. J. L. Morton, High-Cooperativity Coupling of a Rare-Earth Spin Ensemble to a Superconducting Resonator Using Yttrium Orthosilicate as a Substrate, *Phys. Rev. Appl.* **11**, 054082 (2019).
- [23] E. Fraval, M. J. Sellars, and J. J. Longdell, Method of Extending Hyperfine Coherence Times in Pr<sup>3+</sup>: Y<sub>2</sub>SiO<sub>5</sub>, *Phys. Rev. Lett.* **92**, 077601 (2004).
- [24] C. W. Zollitsch, J. O'Sullivan, O. Kennedy, G. Dold, and J. J. L. Morton, Tuning high-q superconducting resonators by magnetic field reorientation, *AIP Adv.* **9**, 125225 (2019).
- [25] S. Weichselbaumer, P. Natzkin, C. W. Zollitsch, M. Weiler, R. Gross, and H. Huebl, Quantitative Modeling of Superconducting Planar Resonators for Electron Spin Resonance, *Phys. Rev. Appl.* **12**, 024021 (2019).
- [26] See Supplemental Material at <http://link.aps.org/supplemental/10.1103/PhysRevB.106.245416> for details of the experimental setup, additional information about the spin system, further details on the coupling between the resonator and the spins and descriptions on theoretical details on methods used in the analysis in the main text.
- [27] E. Abe, H. Wu, A. Ardavan, and J. J. L. Morton, Electron spin ensemble strongly coupled to a three-dimensional microwave cavity, *Appl. Phys. Lett.* **98**, 251108 (2011).
- [28] E. Z. Cruzeiro, A. Tiranov, I. Usmani, C. Laplane, J. Lavoie, A. Ferrier, P. Goldner, N. Gisin, and M. Afzelius, Spectral hole lifetimes and spin population relaxation dynamics in neodymium-doped yttrium orthosilicate, *Phys. Rev. B* **95**, 205119 (2017).
- [29] G. Wolfowicz, A. M. Tyryshkin, R. E. George, H. Riemann, N. V. Abrosimov, P. Becker, H.-J. Pohl, M. L. Thewalt, S. A. Lyon, and J. J. Morton, Atomic clock transitions in silicon-based spin qubits, *Nat. Nanotechnol.* **8**, 561 (2013).
- [30] A. Schweiger and G. Jeschke, *Principles of Pulse Electron Paramagnetic Resonance* (Oxford University Press, Oxford, 2001).
- [31] A. M. Tyryshkin, S. Tojo, J. J. L. Morton, H. Riemann, N. V. Abrosimov, P. Becker, H.-J. Pohl, T. Schenkel, M. L. W. Thewalt, K. M. Itoh, and S. A. Lyon, Electron spin coherence exceeding seconds in high-purity silicon, *Nat. Mater.* **11**, 143 (2012).
- [32] H.-J. Lim, S. Welinski, A. Ferrier, P. Goldner, and J. J. L. Morton, Coherent spin dynamics of ytterbium ions in yttrium orthosilicate, *Phys. Rev. B* **97**, 064409 (2018).
- [33] S. D. Sarma, R. de Sousa, X. Hu, and B. Koiller, Spin quantum computation in silicon nanostructures, *Solid State Commun.* **133**, 737 (2005).
- [34] S. Takahashi, R. Hanson, J. van Tol, M. S. Sherwin, and D. D. Awschalom, Quenching Spin Decoherence in Diamond through Spin Bath Polarization, *Phys. Rev. Lett.* **101**, 047601 (2008).
- [35] M. Rančić, M. L. Dantec, S. Lin, S. Bertaina, T. Chanière, D. Serrano, P. Goldner, R. B. Liu, E. Flurin, D. Estève, D. Vion, and P. Bertet, Electron-spin spectral diffusion in an erbium doped crystal at millikelvin temperatures (2022).
- [36] Y. Sun, T. Böttger, C. W. Thiel, and R. L. Cone, Magnetic *g* tensors for the <sup>4</sup>I<sub>15/2</sub> and <sup>4</sup>I<sub>13/2</sub> states of Er<sup>3+</sup>: Y<sub>2</sub>SiO<sub>5</sub>, *Phys. Rev. B* **77**, 085124 (2008).
- [37] S. Welinski, A. Ferrier, M. Afzelius, and P. Goldner, High-resolution optical spectroscopy and magnetic properties of Yb<sup>3+</sup> in Y<sub>2</sub>SiO<sub>5</sub>, *Phys. Rev. B* **94**, 155116 (2016).
- [38] B. Car, L. Veissier, A. Louchet-Chauvet, J.-L. Le Gouët, and T. Chanière, Optical study of the anisotropic erbium spin flip-flop dynamics, *Phys. Rev. B* **100**, 165107 (2019).
- [39] S. Stoll and A. Schweiger, EasySpin, a comprehensive software package for spectral simulation and analysis in EPR, *J. Magn. Reson.* **178**, 42 (2006).
- [40] V. Ranjan, S. Probst, B. Albanese, A. Doll, O. Jacquot, E. Flurin, R. Heeres, D. Vion, D. Esteve, J. Morton, and P. Bertet, Pulsed electron spin resonance spectroscopy in the Purcell regime, *J. Magn. Reson.* **310**, 106662 (2020).
- [41] L. A. O'Dell, The worst kind of pulses in solid-state nmr, *Solid State Nucl. Magn. Reson.* **55–56**, 28 (2013).
- [42] M. Šimėnas, J. O'Sullivan, O. W. Kennedy, S. Lin, S. Fearn, C. W. Zollitsch, G. Dold, T. Schmitt, P. Schüffelgen, R.-B. Liu, and J. J. L. Morton, Near-Surface <sup>125</sup>Te<sup>+</sup> Spins with Millisecond Coherence Lifetime, *Phys. Rev. Lett.* **129**, 117701 (2022).
- [43] W.-L. Ma, G. Wolfowicz, S.-S. Li, J. J. L. Morton, and R.-B. Liu, Classical nature of nuclear spin noise near clock transitions of Bi donors in silicon, *Phys. Rev. B* **92**, 161403(R) (2015).
- [44] P. Stevenson, C. M. Phenicie, I. Gray, S. P. Horvath, S. Welinski, A. M. Ferrenti, A. Ferrier, P. Goldner, S. Das, R. Ramesh, R. J. Cava, N. P. de Leon, and J. D. Thompson, Erbium-implanted materials for quantum communication applications (2021).
- [45] S. Kanai, F. J. Heremans, H. Seo, G. Wolfowicz, C. P. Anderson, S. E. Sullivan, M. Onizhuk, G. Galli, D. D. Awschalom, and H. Ohno, Generalized scaling of spin qubit coherence in over 12,000 host materials, *Proc. Natl. Acad. Sci. USA* **119**, e2121808119 (2022).